



CHORUS

This is the accepted manuscript made available via CHORUS. The article has been published as:

Real-Frequency Response Functions at Finite Temperature

I. S. Tupitsyn, A. M. Tselik, R. M. Konik, and N. V. Prokof'ev

Phys. Rev. Lett. **127**, 026403 — Published 9 July 2021

DOI: [10.1103/PhysRevLett.127.026403](https://doi.org/10.1103/PhysRevLett.127.026403)

Real-frequency response functions at finite temperature

I. S. Tupitsyn,¹ A. M. Tsvetik,² R. M. Konik,² and N. V. Prokof'ev¹

¹*Department of Physics, University of Massachusetts, Amherst, MA 01003, USA*

²*Condensed Matter Physics and Materials Science Division,
Brookhaven National Laboratory, Upton, NY 11973-5000, USA*

Building on previous developments [1–3], we show that the Diagrammatic Monte Carlo technique allows to compute finite temperature response functions directly on the real-frequency axis within any field-theoretical formulation of the interacting fermion problem. There are no limitations on the type and nature of the system's action or whether partial summation and self-consistent treatment of certain diagram classes are used. In particular, by eliminating the need for numerical analytic continuation from a Matsubara representation, our scheme allows to study spectral densities of arbitrary complexity with controlled accuracy in models with frequency-dependent effective interactions. For illustrative purposes we consider the problem of the plasmon line-width in a homogeneous electron gas (jellium).

Introduction. The promise of the Diagrammatic Monte Carlo (DiagMC) technique—stochastic sampling of high-order connected Feynman diagrams with extrapolation to the infinite diagram order limit—in solving the computational complexity problem for interacting fermions [4] ultimately rests on our ability to formulate a field-theoretical approach with a quickly converging series expansion. As is often the case in the strongly correlated regime, an expansion based on the original interaction potentials, V_0 , and “bare” fermion propagators, G_0 , does not converge. To proceed, the problem is transformed identically by incorporating certain classes of diagrams and interaction effects into an alternative “starting point”. This introduces new effective propagators, \tilde{G} , interactions, U , and counter terms, Λ , in terms of which an alternative diagrammatic expansion is formulated. Shifted and homotopic action tools [5, 6] allow to achieve this goal generically by expressing final answers as Taylor series in powers of the auxiliary parameter ξ , with $\xi = 1$ corresponding to the original problem, and ensuring that the resulting series converge for any $\xi < 1$.

To connect finite-temperature calculations with experimental probes not based on thermodynamic potentials, one needs to compute response functions at real frequencies, or spectral densities. The notorious problem faced by simulations performed in the Matsubara representation is a need for a numerical analytic continuation (NAC) procedure from the imaginary to the real-frequency domain. In general, NAC is only meaningful conditionally (by imposing constraints on the answer), and even extraordinary accurate Monte Carlo (MC) data cannot help resolve fine spectral features following broad lower-frequency peaks, or narrow Drude peaks in optical conductivity [7]. Until recently, the infamous NAC problem standing on the way of the accurate theoretical description of experimentally relevant observables was considered unavoidable.

The breakthrough development in the context of the DiagMC technique was reported in Ref. [1] for the Hubbard model. The key observation was that for expansions

in terms of G_0 and V_0 , the summation over all internal fermionic Matsubara frequencies, $\omega_n = 2\pi T(n + 1/2)$ with integer n , can be performed analytically with the help of the Cauchy formula

$$T \sum_n \left(\prod_{j=1}^M \frac{1}{i\omega_n - a_j} \right) = \sum_{j=1}^M n_j \left(\prod_{s \neq j}^M \frac{1}{a_j - a_s} \right), \quad (1)$$

and automated for arbitrary high-order diagrams. Here $n_j \equiv n(a_j) = [e^{a_j/T} + 1]^{-1}$ is the Fermi-Dirac function. Bose-Einstein function is related to $n(a)$ by $N(a) = -n(a + i\pi T)$. Thus, summation over bosonic frequency ω_m is included in Eq. (1) by the transformation $i\omega_m - a = i\omega_{m+1/2} - a'$ with $a' = a + i\pi T$. [For the imaginary time implementation see Refs. [3, 8].] The Wick rotation of external frequency from the imaginary to the real axis is then performed analytically by replacing $i\Omega_s$ with $\Omega + i\eta$, where $\eta \rightarrow 0$ is positive. The remaining integrals/sums are sampled by Monte Carlo to compute spectral densities directly without any need for NAC. [The proposed below scheme allows to take the $\eta \rightarrow 0$ limit analytically, see Supplemental material [9].]

The entire procedure relies on (i) the simple pole structure of the bare Green's function, $G_0 = (i\omega_n - \epsilon_{\mathbf{k}} + \mu)^{-1}$, where $\epsilon_{\mathbf{k}}$ is the bare dispersion relation and μ is the chemical potential (we suppress the spin index for brevity), and (ii) a frequency independent interaction potential V_0 . These requirements are not satisfied when the diagrammatic expansion is performed in terms of dressed/renormalized propagators and retarded effective interactions to produce convergent series in the strongly correlated regimes. Even if \tilde{G} and U have transparent analytical structure in the Matsubara representation, the summation over all internal Matsubara frequencies cannot be performed analytically any more. For example, in the random phase approximation (RPA) for the homogeneous electron gas (jellium), the polarization operator in the effective screened interaction, $U^{-1} = V_0^{-1} - \Pi$, is approximated by the finite-temperature version of the Lindhard function [10]. No diagram with these U -lines

can be summed over Matsubara frequencies analytically.

It appears that conditions for performing real-frequency simulations are incompatible with the generic tools needed to obtain convergent series expansions. In this work we present a simple solution to this dilemma and formulate an approach that allows to compute real-frequency response functions within an arbitrary field-theoretical setup. To demonstrate how our approach works in practice, we compute the plasmon line-width, γ_{pl} , in the jellium model as a function of momentum and temperature. The problem of plasmon decay is under active study because of its importance for optoelectronics, photovoltaics, photocatalysis, and other applications (see, for instance, Refs. [11–17] and literature therein). Contrary to solid state materials where inter-band transitions and Umklapp processes are possible (and thus the plasmon line-width can be obtained within the lowest skeleton order diagrams, in the so-called GW approximation - see, for instance, Refs. [18, 19]), we find that meaningful results for γ_{pl} in jellium crucially depend on vertex corrections.

Real-frequency finite-temperature technique. To perform the Wick rotation by the substitution $i\Omega_s \rightarrow \Omega + i\eta$, the function in question has to be known analytically. The key observation leading to solution is that at any point in the DiagMC simulation, the propagators and interactions used to express the diagram's contribution are assumed to be *known*, either analytically or numerically (from relatively simple auxiliary simulations). The first step is to convert this knowledge into spectral densities and use them to express \tilde{G} and U via

$$\tilde{G}(\mathbf{k}, i\omega_n) = \frac{1}{\pi} \int_{-\infty}^{\infty} du \frac{A(\mathbf{k}, u)}{i\omega_n - u}; \quad (2)$$

$$U(\mathbf{k}, i\omega_s) = V_0(k) + \frac{1}{\pi} \int_{-\infty}^{\infty} dv \frac{D(\mathbf{k}, v)}{i\omega_s - v}, \quad (3)$$

with bosonic Matsubara frequencies $\omega_s = 2\pi Ts$. The second step is to rewrite all diagrammatic contributions in terms of the A and D functions. This will add integrations over a set of u and v variables on top of momentum (spin) integrations (sums), which is not a problem for Monte Carlo methods. However, the dependence of the integrand on Matsubara frequencies is again a *product of simple poles*, meaning that exact summation over all internal Matsubara indexes can be performed analytically and the result rotated to the real-frequency axis. [Writing all propagators and effective interactions in terms of spectral representations brings additional technical advantages, see [9].]

Equations (2), (3) were used in Ref. [2] for solving the self-consistent GW-approximation at $T = 0$. More importantly, spectral representation for the Green's function was employed in Ref. [3] in the context of Anderson impurity model to compute the real-frequency response using analytic Matsubara integration. However, it was not realized that taken together Eqs. (1)-(3) offer a

generic solution for obtaining real-frequency response in an arbitrary field-theoretical formulation of the interacting many body problem, including cases with frequency-dependent effective interactions.

The rest of this work is devoted to the explicit demonstration of how the proposed scheme works in practice by considering the problem of the plasmon life-time in jellium.

Starting point. First, we need to construct \tilde{G} and U . The jellium model is defined as the homogenous electron gas on a positive neutralizing background

$$H = \sum_i \frac{k_i^2}{2m} + \sum_{i < j} \frac{e^2}{|\mathbf{r}_i - \mathbf{r}_j|} - \mu N, \quad (4)$$

with m the electron mass. In Fourier representation the bare interaction potential is given by $V_0 = 4\pi e^2/q^2$. We use the inverse Fermi momentum, $1/k_F$, and Fermi energy, $\varepsilon_F = k_F^2/2m$, as units of length and energy, respectively, and employ the short-hand notation, $\sum_{\mathbf{k}} = (2\pi)^{-3} \int d^3k$, for momentum integrals. The definition of the Coulomb parameter r_s in terms of the system number density, ρ , and Bohr radius is standard: $4\pi r_s^3/3 = 1/\rho a_B^3$.

Following Ref. [20] in the Matsubara domain, we expand on top of the self-consistent Hartree-Fock solution for the Green's function, and tune the chemical potential to obtain the desired value of r_s . To avoid divergent Fermi-velocity renormalization, this solution is based on the Yukawa potential, $Y(q) = 4\pi e^2/(q^2 + \kappa^2)$, with appropriately chosen parameter κ [see discussion below Eq. (8)]. To be specific, $\tilde{G}^{-1}(\mathbf{k}, i\omega_n) = i\omega_n - \epsilon_{\mathbf{k}}$, where the renormalized dispersion relation $\epsilon_{\mathbf{k}} = k^2/2m - \mu + \Sigma_F(\mathbf{k})$ is iterated using relations $\Sigma_F(\mathbf{k}) = \sum_{\mathbf{q}} Y(\mathbf{q})n(\epsilon_{\mathbf{k}-\mathbf{q}})$, see Fig. 1(a), and $2 \sum_{\mathbf{k}} n(\epsilon_{\mathbf{k}}) = \rho$, until convergence.

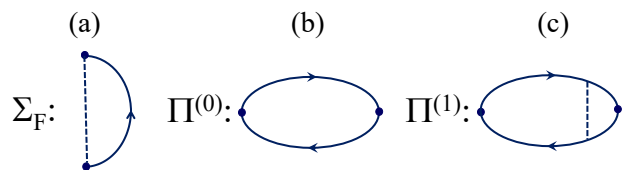


FIG. 1. (color online) (a) Fock self-energy diagram; (b)-(c) 0-th and 1-st order (with respect to the number of interaction lines) contributions to the polarization operator Π . Solid and dashed lines represent the fermionic propagators, \tilde{G} , and Yukawa potentials, Y , respectively.

The same Yukawa potential was used in Ref. [20] in place of the effective interaction potential in the full diagrammatic expansion. This choice is not suitable for our purposes because the plasmon is a collective excitation; an expansion in powers of Y will fail to describe a basic process, $P \rightarrow P + e - h$, where the plasmon is losing its energy by emitting electron-hole pairs, unless certain geometrical series are summed up to infinity.

These considerations force one to consider effective interactions based on dynamic screening effects with “built in” plasmon excitations (see also Section II of the Supplemental material [9]). It is tempting to start with $U^{-1} = V_0^{-1} - \Pi^{(0)}$, where $\Pi^{(0)}$ is given by the diagram shown in Fig. 1(b). However, the resulting plasmon spectrum (derived from the standard condition $U^{-1}(Q, \omega_{pl}) = 0$) strongly violates an exact hydrodynamic relation $\omega_{pl}^2(Q = 0) = \Omega_{pl}^2 = 4\pi e^2 \rho / m$ for translation invariant systems. This problem is eliminated by adding the leading vertex correction, $U^{-1} = V_0^{-1} - \Pi^{(0)} - \Pi^{(1)}$, see Fig. 1(c). The upper inset in the left panel of Fig. 2 shows that now the plasmon spectrum exhibits the proper behavior at $Q \rightarrow 0$, following the standard RPA result in this limit.

To complete the setup, we need to compute the spectral density D in Eq. (3). For this it is sufficient to know the real and imaginary parts of $\tilde{\Pi} = \Pi^{(0)} + \Pi^{(1)} = R + iI$ on the real frequency axis. If we split the total spectral density into the electron-hole continuum, D_{e-h} , and the singular plasmon pole contribution, D_{pl} , then (see also Ref. [21])

$$D_{e-h} = -\frac{I}{[(V_0^{-1} - R)^2 + I^2]}; \quad (5)$$

$$D_{pl} = \pi r_{pl}(Q) \delta(\Omega - \omega_{pl}(Q)) \quad \text{if} \quad I(Q) = 0, \quad (6)$$

where $r_{pl} = 1/|\partial R/\partial \Omega|_{\omega_{pl}(Q)}$ is the pole residue. After summation over Matsubara frequencies, the real-frequency result for $\tilde{\Pi}$ reads:

$$\tilde{\Pi} = -2 \sum_{\mathbf{p}} \mathcal{F}_{\mathbf{p}+\mathbf{Q}, \mathbf{p}} - 2 \sum_{\mathbf{p}, \mathbf{k}} Y(\mathbf{p}-\mathbf{k}) \mathcal{F}_{\mathbf{p}+\mathbf{Q}, \mathbf{p}} \mathcal{F}_{\mathbf{k}+\mathbf{Q}, \mathbf{k}}, \quad (7)$$

$$\mathcal{F}_{\mathbf{q}_1, \mathbf{q}_2} = \frac{n_{\mathbf{q}_1} - n_{\mathbf{q}_2}}{\Omega - \epsilon_{\mathbf{q}_1} + \epsilon_{\mathbf{q}_2} + i\eta}. \quad (8)$$

We evaluated momentum integrals in Eq. (7) by standard Monte Carlo methods on a dense mesh of Q and Ω points for several values of κ . The optimized perturbation theory strategy [22, 23] would be to choose κ in such a way that the answer computed up to a given order of expansion is least sensitive to its arbitrary value. Previous work in this vein [20] considered static properties only. For the fully dynamic calculation, one is further restricted by the condition that the spectral functions need to be positive for any $\Omega > 0$. With respect to the low-frequency behavior, optimal values of κ would correspond to the extrema of the $\tilde{\Pi}(0, 0, \kappa)$ curves, shown in lower insets of Fig. 2 for $r_s = 2$ and $r_s = 4$. The fact that both maxima are broad can be used to choose larger values of κ without loss of accuracy in order to guarantee that $\text{Im}\tilde{\Pi}(\Omega > 0) < 0$. Indeed, unless κ is large enough, $\text{Im}\tilde{\Pi}$ becomes positive in a finite frequency range, see the upper right inset in Fig. 2. Our strategy then is to choose large enough κ as close as possible to the extremum of

$\tilde{\Pi}(0, 0, \kappa)$, leading to $\kappa/k_F = 1.2$ and $\kappa/k_F = 1.8$ for $r_s = 2$ and $r_s = 4$, respectively. The corresponding real and imaginary parts of $\tilde{\Pi}$ are presented in Fig. 2. At moderate values of r_s the qualitative behavior remains similar to that in the RPA. The smoothing of the singularities in the polarization operator is a temperature effect.

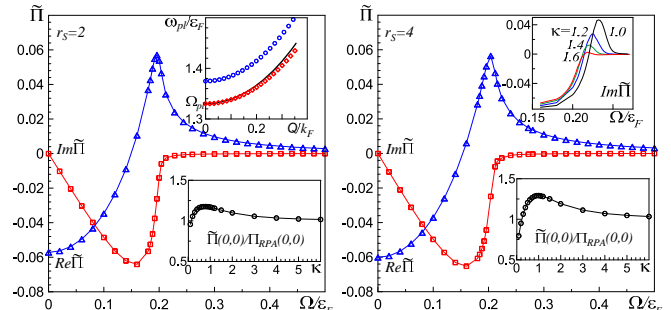


FIG. 2. (color online) Polarization function, $\tilde{\Pi} = \Pi^{(0)} + \Pi^{(1)}$, dependence on frequency at low temperature $T/\epsilon_F = 0.02$. Left panel: $r_s = 2$, $Q/k_F = 0.098437$, $\kappa/k_F = 1.2$. Right panel: $r_s = 4$, $Q/k_F = 0.103711$, $\kappa/k_F = 1.8$. Blue and red curves represent the real and imaginary parts of $\tilde{\Pi}$, respectively. Lower insets show $\tilde{\Pi}(Q = 0, \Omega = 0)/\Pi_{RPA}(Q = 0, \Omega = 0)$ as a function of κ for $r_s = 2$ (left) and $r_s = 4$ (right). In the limit $\kappa \rightarrow \infty$ $\Pi(0, 0)$ saturates at $3\rho/2\epsilon_F$ equal to 0.05066 in our units. The upper left inset shows the low-momentum part of the plasmon dispersion for $r_s = 2$ within the (i) RPA (solid black curve), (ii) $\tilde{\Pi} = \Pi^{(0)}$ approximation (blue circles), and (iii) $\tilde{\Pi}$ with vertex correction (red diamonds). The upper right inset shows how $\text{Im}\tilde{\Pi}$ for $r_s = 4$ changes sign for $\kappa/k_F < 1.8$. All error bars are smaller than symbol sizes.

Plasmon line-width. In our formulation, the lowest-order polarization diagrams contributing to the finite plasmon life-time are shown in Fig. 3. To avoid double-counting, one has to subtract Yukawa potentials from effective screened interactions, because the corresponding contributions are already included in the definitions of \tilde{G} and U functions. The sum of all diagrams in Fig. 3 will be denoted as $\Delta\Pi$.

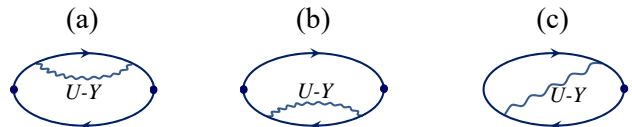


FIG. 3. (color online) Lowest-order polarization diagrams within the formulation based on \tilde{G} and U .

Accounting for the first two diagrams in Fig. 3 would be equivalent to using the so-called GW-approximation perturbatively. It is not surprising then that these two contributions strongly violate another exact hydrodynamic condition, $\Pi(Q \rightarrow 0, \Omega \neq 0) \propto Q^2$, see Ref. [24], because a similar situation takes place in the GW-approximation [2, 25]. If we were to compute the plasmon

line-width on the basis of the first two diagrams in Fig. 3, we would find that the plasmon excitation is completely destroyed at small momenta. Indeed, the data presented in the left panel of Fig. 4 extrapolate to finite values at $Q = 0$, leading to a divergent contribution after multiplication by the Coulomb potential (see also Fig.4 of the Supplemental material [9]).

It is thus crucial not to miss the vertex correction given by the diagram (c) in Fig. 3. It compensates diagrams (a) and (b) almost perfectly for all values of Q , and restores the proper $\propto Q^2$ behavior of the (a)+(b)+(c) sum at small momenta, see right panel of Fig. 4. The involved analytical expressions for all diagrams (before Monte Carlo integration over internal momenta) can be found in the Supplemental material [9] (see Section I). While their derivation on the basis of Cauchy formula (1) is straightforward, the number of terms rapidly increases with the number of frequency dependent lines, not to mention that U functions (3) contain three distinct contributions: frequency independent part, plasmon pole, and electron-hole continuum.

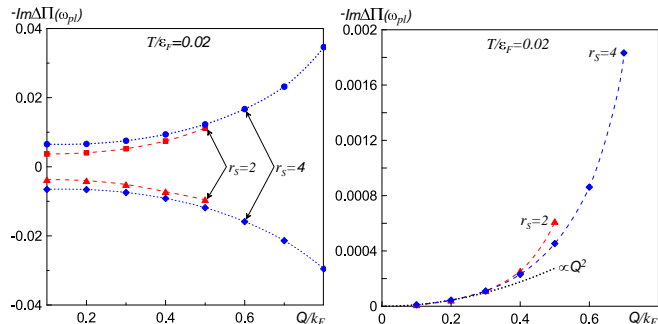


FIG. 4. (color online) Minus imaginary part of the polarization operator contributions pictured in Fig. 3 as functions of momentum for $\Omega = \omega_{pl}(Q)$ and $T/\varepsilon_F = 0.02$. Left panel: Upper curves are contributions from the sum of diagrams (a) and (b) for $r_s = 2$ (dashed with squares), and $r_s = 4$ (dotted with circles). Lower curves are contributions from the diagram (c) for $r_s = 2$ (dashed with triangles), and $r_s = 4$ (dotted with diamonds) Right panel: The sum of diagrams (a), (b), and (c) for $r_s = 2$ (red dashed curve with triangles) and $r_s = 4$ (blue dashed curve with diamonds). The Q^2 -dependence (black dotted curve) is added for comparison. All error bars are smaller than symbol sizes.

After evaluating the imaginary part of $\Delta\Pi(Q, \Omega = \omega_{pl}(Q))$ we obtain the plasmon line-width from

$$\gamma_{pl}(Q, T) = -r_{pl}(Q, T) \text{Im}\Delta\Pi(Q, \omega_{pl}(Q, T), T). \quad (9)$$

[At small momenta $r_{pl} \approx V_0 \omega_{pl}/2 \propto Q^{-2}$.] Since the final result for γ_{pl} is much smaller than ω_{pl} there is no need for performing a frequency scan. We have verified that the answer does not change when $Im\Delta\Pi$ is computed at frequencies $\omega_{pl} \pm \gamma_{pl}$.

Our final results for the plasmon line-width on the basis of diagrams with one U -line are discussed in

Fig. 5. All data are presented as dimensionless ratios $\gamma_{pl}(Q, T)/\omega_{pl}(Q, T)$ to immediately see when plasmon excitations remain well-defined. This appears to be the case all the way to the plasmon spectrum end point for both values of r_s when the temperature is low. The line-width saturates to a finite value in the $Q \rightarrow 0$ limit because the Q^2 -dependence of $Im\Delta\Pi$ is compensated by the divergence of the Coulomb potential present in the definition of the plasmon residue.

The answer is also finite in the $T \rightarrow 0$ limit. This can be understood on the basis of spectral density for two ($e - h$) excitations that overlaps with the plasmon peak [21]. Thus there exist kinematically allowed decay channels for $Q = 0$ plasmons excited from the ground state of the system. Somewhat surprising is the fact that the line-width remains rather small even for large values of r_s . Finite-temperature corrections are linear at values $T/\varepsilon_F \ll 1$ with a much stronger temperature dependence emerging at $T/\varepsilon_F > 1$.

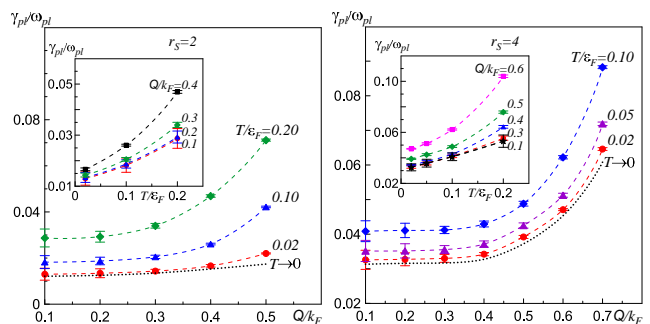


FIG. 5. (color online) Plasmon line-width to plasmon frequency ratio as a function of momentum at different temperatures for $r_s = 2$ (left panel) and 4 (right panel). The black dotted lines in both panels show results extrapolated to the $T \rightarrow 0$ limit using parabolic fits. Temperature dependence for different values of Q is shown in insets.

Higher order contributions. Our reformulation of the diagrammatic expansion in terms of \hat{G} and U is exact, and one can proceed with computing higher-order diagrams using standard rules. We illustrate some of the second-order diagrams and process them in the Supplemental material [9] (see Section III). While summation over internal Matsubara frequencies allows to perform calculations directly on the real-frequency axis, it also brings additional computational challenges. Using two next-order diagrams as an example, in [9] we demonstrate that processing Matsubara sums “by hand” quickly leads to expressions of overwhelming complexity (the remaining momentum integrals are done by standard Monte Carlo techniques). Since the Cauchy formula (1) is recursive, it should be possible to fully automate the process, similarly to what was done in Ref. [1] for the case when only fermionic propagators were frequency dependent.

Given that certain groups of diagrams feature strong compensation, an efficient algorithm would need to com-

bine them analytically (see also Ref. [20]). We see clear advantages in implementing the recursive scheme for obtaining Taylor expansions from skeleton diagrams [26], because it automatically groups irreducible diagrams and reduces the number propagators and interaction lines. This scheme also significantly simplifies processing of counter terms, and eliminates higher order poles in Mutsubara sums.

Conclusion. Building on previous developments [1–3], we report a solution to the problem of computing finite-temperature response functions on the real frequency axis using Feynman diagrams for an arbitrary field-theoretical formulation of the interacting problem. This includes problems with frequency-dependent effective interactions and dressed, renormalized, or self-consistent treatments required for producing convergent expansions. Spectral densities (of arbitrary complexity) for experimentally relevant observables (optical conductivity, resonant inelastic X-ray spectroscopy, neutron scattering, excitation life-times, etc.) can be computed with an accuracy that was never possible before. Realistically, contribution from diagrams up to sixth order may be reached.

To illustrate how the technique works, we used it to compute the leading processes contributing to the finite plasmon line-width within the jellium model, and studied the line-width dependence on momentum and temperature for moderate values of the Coulomb parameter r_s . The increase of the interaction strength leads to a decrease of the plasmon life-time, but nevertheless the plasmon remains well defined. One important qualitative result is the necessity to include vertex corrections in order to ensure the obtained results do not violate general principles. Future work will aim at developing efficient schemes for generating and processing real-frequency expressions for high-order diagrams to gain full control over systematic errors resulting from the series truncation.

Acknowledgements. AMT, RMK, and IST thank support from the Office of Basic Energy Sciences, Material Sciences and Engineering Division, U.S. Department of Energy under Contract No. DE-SC0012704. NVP thanks support from the Simons Collaboration on the Many Electron Problem. The authors thank James LeBlank and Kun Chen for sharing details on their methods and helpful discussions.

-
- [1] A. Taheridehkordi, S.H. Curnoe, and J.P.F. LeBlanc, Phys. Rev. **B 99**, 035120 (2019); Phys. Rev. **B 101**, 125109 (2020); Phys. Rev. **B 102**, 045115 (2020).
 - [2] B. Holm and U. von Barth, Phys. Rev. **B 57**, 2108 (1998).
 - [3] J. Vičičević and M. Ferrero, Phys. Rev. **B 101**, 075113 (2020).
 - [4] R. Rossi, N. Prokof'ev, B. Svistunov, K. Van Houcke, and F. Werner, Euro Phys. Lett. **118**, 10004 (2017).
 - [5] R. Rossi, F. Werner, N. Prokof'ev, B. Svistunov, Phys. Rev. **B 93**, 161102(R) (2016).
 - [6] A. J. Kim, N. V. Prokof'ev, B. V. Svistunov, and E. Kozik, arXiv:2010.05301
 - [7] O. Goulko, A.S. Mishchenko, L. Pollet, N. Prokof'ev, and B. Svistunov, Phys. Rev. **B 95**, 014102 (2017).
 - [8] J. Vičičević, P. Stipsić, and M. Ferrero, arXiv:2011.08226.
 - [9] Supplemental material
 - [10] J. Lindhard, Mat. Fys. Medd. K. Dan. Vidensk. Selsk, **28**, 1 (1954).
 - [11] J. M. Luther and J. L. Blackburn, Nat. Photonics **7**, 675 (2013).
 - [12] C. Clavero, Nat. Photonics **8**, 95 (2014).
 - [13] H. A. Atwater and A. Polman, Nat. Mater. **9**, 205 (2010).
 - [14] S. Linic, P. Christopher, and D. B. Ingram, Nat. Mater. **10**, 911 (2011).
 - [15] S. Mukherjee, F. Libisch, N. Large, O. Neumann, L. V. Brown, J. Cheng, J. B. Lassiter, E. A. Carter, P. Nordlander, and N. J. Halas, Nano Lett. **13**, 240 (2013).
 - [16] W. Li and J.G. Valentine, Nanophotonics **6**(1), 177, (2017).
 - [17] K. Kolwas, Plasmonics **14**, 1629 (2019).
 - [18] M. Bernardi, J. Mustafa, J.B. Neaton and S.G. Louie, Nat. Commun. **6**, 7044 (2015).
 - [19] R. Sundararaman, P. Narang, A.S. Jermyn, W.A. Goddard III and Harry A. Atwater, Nat. Commun. **5**, 5788 (2014).
 - [20] K. Chen and K. Haule, Nat. Commun. **10**, 3725 (2019); *ibid.* arXiv:2012.03146.
 - [21] I.S. Tupitsyn, A.M. Tselik, R.M. Konik, N.V. Prokof'ev, Phys. Rev. **B**, 102 (7), 075140 (2020).
 - [22] P.M. Stevenson, Phys. Rev. **D 23**, 2916 (1981).
 - [23] R.P. Feynman and H.E. Kleinert, Phys. Rev. **A 34**, 5080 (1986).
 - [24] P. Nozieres and D. Pines, *Theory Of Quantum Liquids*, Chapters 2 and 3, Westview Press (1999).
 - [25] K.V. Houcke, I.S. Tupitsyn, A.S. Mishchenko, N.V. Prokof'ev, Phys. Rev. **B 95** (19), 195131 (2017).
 - [26] W. Wu, M. Ferrero, A. Georges, and E. Kozik, Phys. Rev. **B 96**, 041105 (2017)